

Resonant X-ray Emission of Hexagonal Boron Nitride

John Vinson,^{1,*} Terrence Jach,¹ Matthias Müller,² Rainer Unterumsberger,² and Burkhard Beckhoff²

¹*Material Measurement Laboratory, National Institute of Standards and Technology, Gaithersburg, MD 20899*

²*Physikalisch-Technische Bundesanstalt, Abbestraße 2-12, 10587 Berlin, Germany*

(Dated: November 6, 2017)

The electronic structure of hexagonal boron nitride (*h*-BN) is explored using measurements of x-ray absorption and resonant inelastic x-ray scattering (RIXS) at the nitrogen K edge (1s) in tandem with calculations using many-body perturbation theory within the *GW* and Bethe-Salpeter equation (BSE) approximations. Our calculations include the effects of lattice disorder from phonons activated thermally and from zero point energy. They highlight the influence of disorder on near-edge x-ray spectra.

I. INTRODUCTION

Boron nitride commonly occurs in two crystalline phases: *sp*³-bonded cubic (diamond-like) and *sp*²-bonded hexagonal (graphitic). It can also exist in wurtzite and amorphous bulk phases, and hexagonal boron nitride (*h*-BN) can be synthesized both as a single layer (graphene-like) and in nanotubes [1, 2]. Bulk and single-layer *h*-BN are of great physical interest, as, unlike graphite and graphene, *h*-BN is a large band gap semiconductor. Many aspects of both the *h*-BN structure and electronic behavior are still not settled. The value of the electronic band gap [3, 4], and the exact stacking order and prevalence of faults remain areas of interest [5].

The electronic structure of boron nitride has been studied computationally now for 40 years, starting with tight-binding models [6, 7], progressing to density functional theory methods [8, 9], and more recently including self-energy effects by way of the *GW* approximation [10, 11]. Experimentally, boron nitride has also been the focus of x-ray absorption and non-resonant emission studies [12–15]. Resonant inelastic x-ray scattering (RIXS) experiments on *h*-BN have also been carried out at both the boron edge [15, 16] and later the nitrogen edge [17, 18].

Two competing theoretical frameworks have been used in previous works to model and understand RIXS in *h*-BN. One originated with the work of Ma *et al.* [19, 20] and was later picked up by Jia *et al.* [16] and Shirley *et al.* [21–23]. These papers advanced the view that RIXS should be modeled as a coherent process, conserving crystal momentum **k**. A second approach, outlined in the works of Yanagihara *et al.* [24], Noba *et al.* [25], and Miyata *et al.* [17], focuses on the importance of the spectator electron on the emission spectra when the initial x-ray energy is tuned down to the absorption edge. This second method assumed that coherence is lost through phonon interactions. It relies upon a local framework to model the RIXS process, inherently excluding the consequences of momentum conservation and coherence.

Here we extend the former, coherent approach for modeling RIXS spectra. We assume that the excitation and

deexcitation occurs too fast to involve phonon interactions with the exciton. However, unlike the aforementioned previous studies, we allow the RIXS process to take place in a crystal lattice that is continuously disordered on a slower time scale by the presence of phonons. The disorder includes both thermal and zero-point motion of the atoms. Consequently, the observed spectrum is an incoherent sum of coherent spectra, each generated from a disordered snapshot. Furthermore, we show that the dispersion of the valence bands in *h*-BN is not well described by standard density-functional theory, but this shortcoming can be remedied through self-energy corrections. Both disorder and self-energy corrections are shown to improve the fidelity of the calculated x-ray spectra.

We begin this paper by calculating ground-state properties of *h*-BN in section II. In section II A we investigate the phonon band structure of *h*-BN and evaluate the vibrational disorder in the crystal. We present the electronic quasi-particle band structure in section II B and evaluate the effect of self-energy corrections. We outline the procedures for the experimentally measured and theoretically calculated x-ray spectra in sections III A and III B respectively, and compare calculated and measured x-ray absorption spectra (XAS) and RIXS in III C.

II. GROUND-STATE PROPERTIES

Individual sheets of *h*-BN are isostructural to graphene, but, in contrast to graphite, the layers of bulk *h*-BN stack directly on top of each other, so-called *AA'* stacking, alternating B and N atoms and giving a P6₃/mmc space group. For all of the calculations we use the experimentally determined lattice constants of *a* = 0.2504 nm and *c* = 0.6661 nm [26].

A. Phonon Band Structure and Disorder

As a crystalline system, *h*-BN has long-range order in the average positions of its constituent atoms, but the instantaneous disorder from thermal and zero-point motion can have a significant effect on the optical and x-ray spec-

* john.vinson@nist.gov

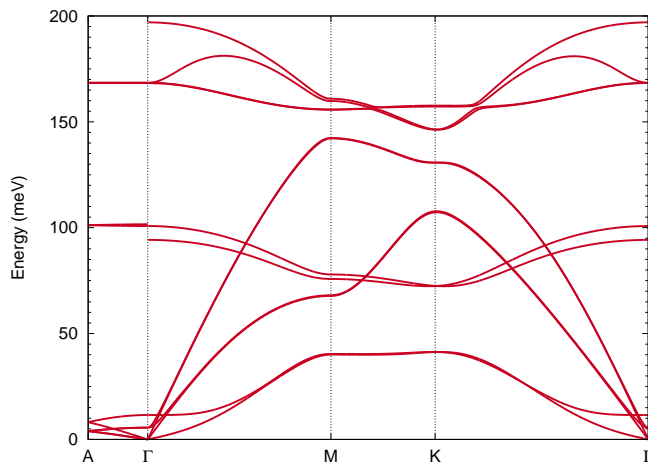


FIG. 1. The phonon band structure of *h*-BN in meV as a function of *q*-vector. High-symmetry points in the Brillouin zone are labeled. Large discontinuities exist at Γ , reflecting differences between in-plane and out-of-plane behavior.

tra. This effect can be modeled by summing calculated absorption and RIXS spectra over a representative ensemble of structures. Previously it was shown that such structures can be generated by considering the phonon modes of the system within a harmonic approximation [27, 28], and this technique has since been independently adopted elsewhere [29]. The advantage of the phonon-mode approach is that the quantum nature of the nuclear wave functions, i.e., zero-point motion, is included automatically, whereas in standard molecular dynamics simulations the nuclei are classical particles. However, unlike molecular dynamics, the phonon-mode approach is limited by the assumption that the nuclei move in harmonic potentials.

We calculated the phonon band structure of *h*-BN using density functional perturbation theory within the QUANTUM ESPRESSO code [30, 31]. The phonon calculation was carried out on a $20 \times 20 \times 6$ *k*-point mesh using ultrasoft pseudopotentials [32] and the local-density approximation (LDA) exchange-correlation potential [33]. Using Fourier interpolation we constructed the band structure shown in Fig. 1. Our calculation agrees well with previous work and measurements [34–36]. The phonon modes span an energy range up to 200 meV. For our experiments, at a temperature of 25 °C, $k_B T = 26$ meV. Note that along *A*– Γ , corresponding to propagation along the *c*-axis, half of the phonon bands are well below $k_B T$.

The phonon-mode approach constructs a disordered supercell by considering the phonon modes of a commensurate grid in reciprocal space, or, equivalently, the Γ -point phonon modes of that supercell. This requirement arises from the periodic boundary conditions. An incommensurate phonon wavevector would lead to discontinuities across the boundaries of the supercell. The phonon-mode approach, therefore, necessarily reduces the disorder

of the system that can be sampled by including only a limited number of modes. Discounting at present the harmonic approximation, which eliminates higher-order terms in the potential energy surface (cubic, quartic, etc.) as well as phonon-phonon terms, the effect of a finite-sized supercell should be similar between phonon-mode and molecular dynamics approaches.

To investigate the effect of supercell size on disorder we turn to the pair distribution function $g_{AB}(r)$ which is the probability that an atom of type *A* is a distance *r* from an atom of type *B*. For a given phonon mode with index λ and crystal momentum \mathbf{q} , each atom will travel along a one-dimensional path given by $\vec{\xi}_i$, where the full $3N$ dimensional vector ξ is an eigenvector of the dynamical matrix (see Ref 31) and *N* is the number of atoms in the cell. Within the harmonic approximation the probability distribution function for the displacement $\Delta\tau$ of atom *i* due to a single phonon mode λ, \mathbf{q} with frequency ω takes on the form of a Gaussian

$$P_{i,\lambda,\mathbf{q}}(\Delta\tau; T) = \frac{1}{\sqrt{2\pi} u_{i,\lambda,\mathbf{q}}(T)} e^{-\Delta\tau^2/2u_{i,\lambda,\mathbf{q}}^2(T)} \quad (1)$$

$$u_{i,\lambda,\mathbf{q}}^2(T) = \frac{|\vec{\xi}_{i,\lambda,\mathbf{q}}|^2}{M_i \omega_{\lambda,\mathbf{q}}^2} [1/2 + n(\omega_{\lambda,\mathbf{q}}; T)]$$

$$n(\omega_{\lambda,\mathbf{q}}; T) = \left[e^{\omega_{\lambda,\mathbf{q}}/k_B T} - 1 \right]^{-1}.$$

The variance u^2 depends on the magnitude of ξ , the mass of the atom M_i , and the phonon mode's occupation number n . The phonons follow Bose statistics; n varies with temperature *T* scaled by Boltzman's constant k_B . Alternatively we can also formulate the probability distributions \tilde{P} from treating the phonon modes as *classical* harmonic oscillators,

$$\tilde{P}_{i,\lambda,\mathbf{q}}(\Delta\tau; T) = \pi^{-1} \frac{1}{\left(\Delta\tau^2 - A_{i,\lambda,\mathbf{q}}^2(T) \right)^{1/2}} \quad (2)$$

$$A_{i,\lambda,\mathbf{q}}^2(T) = \frac{2k_B T |\vec{\xi}_{i,\lambda,\mathbf{q}}|^2}{M_i \omega_{\lambda,\mathbf{q}}^2},$$

where now each atom is confined by the classical turning points *A*, and, unlike the quantum distribution which has a factor of $1/2$ added to the occupation number, the atomic displacements go to zero at zero temperature.

We generated *N*-*N* and *N*-*B* pair-distribution functions $g(r)$ within the phonon mode approach for an $8 \times 8 \times 4$ (1024-atom) supercell using both the classical and quantum distributions (Fig. 2). As expected there is more structure, sharper peaks in $g(r)$, when the atoms follow classical trajectories, but the inter-plane distributions are similar using quantum or classical statistics due to the presence of low-energy modes corresponding to inter-layer breathing or sliding motions. We also constructed a smaller, $4 \times 4 \times 1$ (64-atom) supercell. As can be seen in Fig. 2, the 64- and 1024-atom supercells give almost identical $g(r)$ within the first 10 a.u. which includes the first nine nearest neighbors. From this we conclude that the

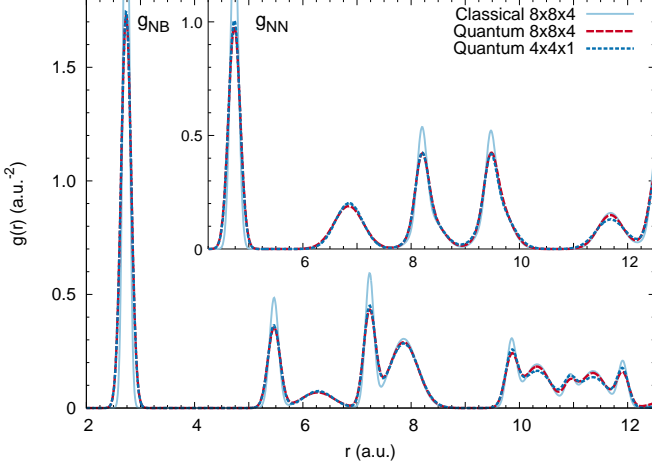


FIG. 2. (color online) The N-B and N-N (inset) pair-distribution functions calculated with the phonon-mode approach using a classical distribution (red, solid) compared to the quantum distribution for both a $8 \times 8 \times 4$ supercell (light-blue, dashed) and a $4 \times 4 \times 1$ supercell (dark-blue, dotted). Cell size has almost no effect through the first 9 nearest neighbors (10 a.u.). For the N-N distributions there are artifacts whenever r is equal to the supercell dimension because the central nitrogen atom will always be the same distance from its images. These have been removed from the plot.

64-atom supercell allows sufficient disorder for near-edge x-ray simulations of *h*-BN.

For *h*-BN (and many systems) a challenge emerges at the Γ -point where the phonon modes are discontinuous and depend on the direction of approach in \mathbf{k} -space (see Fig. 1). We can therefore generate the phonon modes at the Γ -point approaching from in-plane, along M or K, or out-of-plane, along A. Alternatively, both in-plane and out-of-plane derived modes can be considered and averaged appropriately (2:1 ratio). Regardless of how the approach towards Γ is handled, the effect will diminish with increasing supercell size, i.e., as the density of \mathbf{k} -space sampling increases the relative weight of an individual \mathbf{k} -point decreases. We found that for an $8 \times 8 \times 4$ supercell the differences in pair distribution functions between methods were small, $\Delta g(r) < 0.012 \text{ a.u.}^{-2}$. The best agreement for $g_{NB}(r)$ and $g_{NN}(r)$ between the $8 \times 8 \times 4$ and $4 \times 4 \times 1$ supercells was achieved by neglecting LO-TO splitting at Γ , though approaching in-plane (along $M \rightarrow \Gamma$) yields similar results.

B. Electron Band Structure and Self-energy

Green's function methods, such as the Bethe-Salpeter equation (BSE) approach adopted here for calculating XAS and RIXS, hinge upon an accurate approximation to the single-particle Green's function for the electrons in the system. To that end we use density functional theory (DFT) to generate a basis of electron states, but

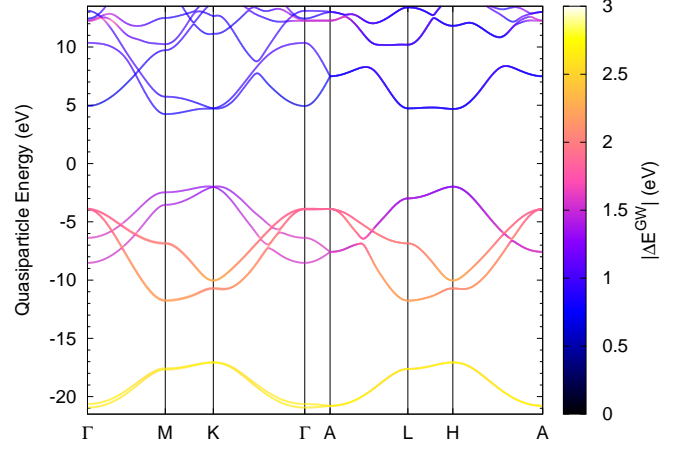


FIG. 3. (color online) The *GW* band structure of *h*-BN in eV as a function of \mathbf{k} -vector. High-symmetry points in the Brillouin zone are labeled. The color of the bands reflects the magnitude of the difference ΔE^{GW} between the *GW* and LDA energies (Eq. 4). Bands are universally shifted away from the Fermi level (1.14 eV) by the *GW* corrections. The valence bands shown differ in their *GW* corrections by $\approx 0.8 \text{ eV}$ – the two π bands (energy minima near Γ) have a smaller correction than the four σ bands (energy maxima near Γ).

DFT, especially within the LDA, is known to have several shortcomings. Specifically band widths and band gaps tend to be underestimated. To assess the reliability of DFT, we first consider many-body self-energy corrections by way of Hedin's *GW* method [37].

The one-electron Green's function G is written in terms of the non-interacting one-electron Green's function G_0 and the frequency-dependent self-energy Σ ,

$$G(\omega, \mathbf{k}) = G_0(\omega, \mathbf{k}) + G_0(\omega, \mathbf{k})\Sigma(\omega, \mathbf{k})G(\omega, \mathbf{k}). \quad (3)$$

In Hedin's formulation, Σ , and hence G , is determined self-consistently via a set of five equations including the screened Coulomb interaction W , the polarizability P , and the vertex Γ . Here we neglect the vertex corrections and only carry out a single iteration ($\Sigma \approx iG^0W^0$). This assumes that the LDA eigenfunctions are “good” representations of the interacting single-particle wave functions ($\langle \psi_{n\mathbf{k}}^{\text{LDA}} | \psi_{n\mathbf{k}}^{\text{GW}} \rangle \approx 1$), and only the eigenenergies are modified by the self-energy operator

$$\begin{aligned} E_{n\mathbf{k}}^{\text{GW}} &= E_{n\mathbf{k}}^{\text{LDA}} + \langle \psi_{n\mathbf{k}}^{\text{LDA}} | \hat{\Sigma}(E_{n\mathbf{k}}^{\text{GW}}) - \hat{V}_{\text{XC}} | \psi_{n\mathbf{k}}^{\text{LDA}} \rangle \\ \Delta E_{n\mathbf{k}}^{\text{GW}} &= \langle \psi_{n\mathbf{k}}^{\text{LDA}} | \hat{\Sigma}(E_{n\mathbf{k}}^{\text{GW}}) - \hat{V}_{\text{XC}} | \psi_{n\mathbf{k}}^{\text{LDA}} \rangle, \end{aligned} \quad (4)$$

where the single-particle wave functions are labeled by band n and crystal momentum \mathbf{k} . Note that the self-energy operator $\hat{\Sigma}$ depends on the quasiparticle energy (and not the DFT energy), and therefore must be self-consistently determined.

Previous calculations of the *GW*-corrected band structure of *h*-BN have been carried out using different plasmon-pole models for the screening [10, 11, 38, 39],

and recently using frequency convolution [40]. We carried out full-frequency calculations of the GW corrections of h -BN using the ABINIT package [41], and we have plotted the GW -corrected band structure in Fig. 3 using Wannier interpolation via the WANNIER90 code [42]. The initial DFT orbitals were calculated within the LDA on a Γ -centered $12 \times 12 \times 4$ \mathbf{k} -point grid. The planewave energy cut-off was set to 56 Ha but downsampled to 20 Ha for the calculation of the polarizability and 22 Ha for the calculation of Σ . The dielectric matrix was constructed with a cut-off of 16 Ha giving 749 plane-waves, while the exchange part of Σ had a cut-off of 26 Ha. For the polarizability 648 bands were included (640 conduction), while 640 total bands were used for the calculation of the self-energy. The dielectric matrix was constructed at 15 imaginary frequencies and 25 real, with 1 eV spacing along the real axis. We estimate the error in G^0W^0 energies from using a finite number of plane-waves, bands, and \mathbf{k} -points to be less than 0.05 eV for the bands plotted and within 0.02 eV for the band gap.

The bands in Fig. 3 are colored by the magnitude of the difference between the LDA and GW energies (Eq. 4). Note, the unit cell contains two formula units, doubling the bands. The GW corrections increase the energy of the unoccupied states and, conversely, decrease the energy of the occupied. An important difference can be seen in the valence bands between the four σ and two π bands between -12 eV and -2 eV. The σ bands have their maximum energy near Γ while the π bands are a half cycle out of phase. The shifts for these two sets differ by about 0.8 eV with the π states undergoing a smaller correction from the GW , indicative of their more diffuse character. Two more tightly bound σ bands are located between -17 eV and -21 eV with a shift of around 2.7 eV.

Our calculations show that within the G^0W^0 approximation h -BN is an indirect band gap semiconductor with a fundamental gap of 6.34(2) eV and an optical gap of 6.80(2) eV located at H ($\frac{1}{3}, \frac{1}{3}, \frac{1}{2}$) compared to LDA gaps of 4.10 eV and 4.51 eV respectively. It should be stressed that this calculation is for a system where the atoms are all at their equilibrium positions – even approaching 0 K a physical system would be subject to zero-point motion which generally reduces the band gap. We find that the bottom of the conduction band is at M ($\frac{1}{2}, 0, 0$) with an energy of 4.30(2) eV. The top of the valence band is $-2.038(20)$ eV located near K ($\frac{1}{3}, \frac{1}{3}, 0$) on the path to M, but a second point near K (along the path to Γ) the valence band reaches $-2.042(20)$ eV which, along with the valence band maximum at H of $-2.054(20)$ eV are all indistinguishable within our estimated uncertainty.

III. X-RAY SPECTRA

A. Experimental setup

The experiments were carried out on the PTB plane grating monochromator (PGM) U49 beamline at the

electron storage ring BESSY II [43]. A description of the monochromator and spherical grating spectrometer geometry has been given before [44, 45]. The spectrometer was oriented in the plane of polarization of the incident beam at a scattering angle of 90° (p-polarization). The energy scale of the plane grating monochromator was again calibrated in the vicinity of the N K edge using the absorption spectrum of an N_2 gas cell as detected by a photodiode. The energy scale of the spectrometer was calibrated using elastic scattering of the excitation radiation. The details of the monochromator and spectrometer energy calibration have been previously described [28].

The sample consisted of a layer of polycrystalline h -BN deposited on a glass substrate, and mounted at 45° from both the incident beam and the spectrometer take-off. All measurements were carried out at room temperature. Absorption spectra were obtained by monitoring the N K line fluorescence intensity with a silicon drift detector (SDD) normal to the sample plane. The fluorescence intensities were corrected for self-absorption in order to have a true x-ray absorption spectrum (XAS). This was done by using a previously obtained, experimental ratio for the same compound of electron escape (short mean free path) vs. total fluorescence (long mean free path) as a function of energy. X-ray emission spectra were accumulated at each excitation energy for 1800 s or 3600 s (normalized to 1800 s).

B. X-ray calculation details

For the x-ray calculations we used both the unit cell as well as 64-atom $4 \times 4 \times 1$ supercells, using the previously stated lattice constants of $a = 0.2504$ nm and $c = 0.6661$ nm [26]. We generated 8 disordered snapshots using the method outlined in section II A. As shown in Fig. 2 this size cell provides sufficient degrees of freedom for disorder. For both the calculated absorption and emission spectra we generate statistical uncertainty estimates, $\Delta\sigma(\omega) = (\sum_i [\sigma(\omega) - \sigma_i(\omega)]^2)^{1/2}/N$, where σ_i is the spectrum from a single configuration and N is the number of configurations averaged together to generate the average spectrum σ . Because the sample was disordered and not a single crystal, the calculated x-ray absorption is an average over three perpendicular polarizations, \hat{x} , \hat{y} , and \hat{z} (in the absence of disorder \hat{x} and \hat{y} would be equivalent). To calculate the RIXS, a total of nine incoming polarizations were used: the three previous plus $(\pm 1, 1, 0)$, $(\pm 1, 0, 1)$, and $(0, \pm 1, 1)$. Note that for the polarization the anti-parallel direction is equivalent, e.g., $(1, 1, 0)$ is the same as $(-1, -1, 0)$. To match the experimental setup, the emission polarization is constrained to be perpendicular to the incoming polarization. For each of the nine initial polarizations emission was calculated for four outgoing polarizations, making for a total of 36 combinations.

We carried out x-ray calculations using the OCEAN

code [46, 47]. Further details on the extension to RIXS with OCEAN can be found in Ref. 28. Norm-conserving pseudopotentials were generated for both boron and nitrogen using the OPIUM code [48]. Where numerical values differ between the disordered supercells and the unit cell we denote the unit-cell values within parentheses (). For the x-ray calculations we sampled the orbitals on a $6 \times 6 \times 10$ ($16 \times 16 \times 4$) \mathbf{k} -point mesh and included 512 (72) conduction bands. The DFT orbitals were generated with QUANTUMESPRESSO [30] using the LDA with a 110 Ry. energy cutoff. The orbitals were downsampled onto a $16 \times 16 \times 12$ ($8 \times 8 \times 20$) real-space grid for the BSE calculation. The core-hole screening is calculated with a 2^3 \mathbf{k} -point grid and 2000 (300) bands. An average optical dielectric constant ϵ_∞ of 4.41 is calculated from the RPA screening at vanishing q , and is in reasonable agreement to the directionally-weighted average of experimental measurements 4.67: 4.10 (4.95) for $E \parallel c$ ($E \perp c$) [49].

Carrying out GW calculations on the disordered supercells was not feasible. The disorder of the supercells reduced the fundamental LDA gap to approximately 3.6(2) eV. Including the approximate GW band-gap correction from the ordered cell gives 5.9(2) eV which compares well with a recent measurement which estimated the single-particle band gap to be 6.08 eV [3], albeit with significant uncertainties in our calculation. Previous optical measurements estimated single-particle gaps of 5.96 eV and 5.971 eV [50, 51]. However, photo-current measurements point to a larger 6.42 eV gap [4], and are consistent with valence BSE calculations that suggested an excitonic binding of 0.7 eV [52], significantly stronger than the values determined in the aforementioned optical measurements.

C. Results

1. X-ray absorption

We show the XAS of h -BN in Fig. 4, including calculations of the ordered unit cell and the average of our disordered $4 \times 4 \times 1$ supercells. The changes in the calculated spectra from introducing disorder are significant. While both the ordered and disordered spectra include 0.1 eV Lorentzian broadening to account for the core-hole lifetime, the unit cell spectrum has been convoluted with a 0.5 eV full-width half-maximum Gaussian to reduce unphysical structure. The 64-atom supercell was convoluted with only a 0.1 eV Gaussian, estimated to match experimental broadening sources separate from the core-hole lifetime effect. Despite this artificial smoothing, the unit-cell spectrum remains much more structured than the spectrum calculated with disorder or the one measured. Additionally, the feature intensities of the ordered cell calculation are much stronger than for the disordered calculation, especially at 407 eV, but this discrepancy is also present at the exciton at 401 eV and higher peak at

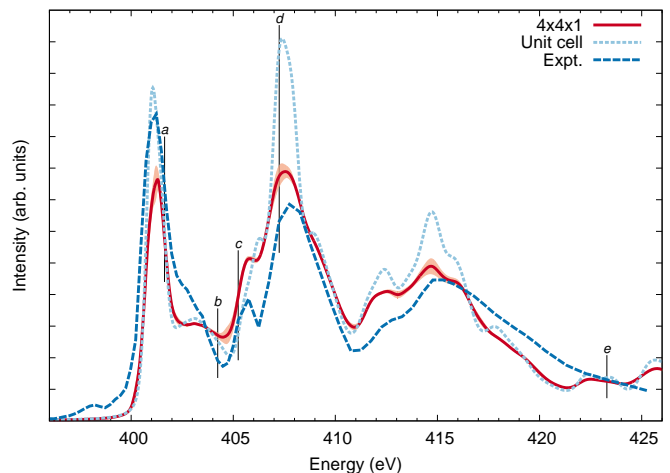


FIG. 4. (color online) The nitrogen K-edge XAS of h -BN calculated using disordered $4 \times 4 \times 1$ supercells (red, solid) and the ordered unit cell (light-blue, dotted), compared against the measured spectrum (dark blue, dashed). Black, vertical lines mark the locations at which emission spectra were taken (see Fig. 5). The orange shaded region around the supercell curve denotes a 95 % confidence interval ($\pm 2\Delta\sigma$) for the uncertainty in the mean from averaging over only 8 configurations.

415 eV. This we attribute to plentiful p -type empty states on the nitrogen atoms, which, due to disorder in the atomic positions, rehybridize slightly, shifting weight to dipole-forbidden s -type. Importantly, while small shifts in atomic position may not strongly change the character of extended, conduction-band electron states, the initial core-level orbitals, and hence the origin for the transition matrix elements, remain centered on the atoms. This can dramatically change the effective character of unoccupied states as seen by dipole-limited x-ray absorption, reducing the spectral weight of allowed states or allowing the observation of previously dark ones. The addition of disorder is seen to improve the agreement with experiment.

Overall the agreement between theory and experiment is quite good for both feature location and intensity. The pre-edge feature at 398 eV, present only in the measured spectrum, is likely molecular N_2 or some other impurity on the sample. There is a significant discrepancy in the spectral weight of the first major feature 401 eV to 404 eV. Further, our measurements are in contrast to the spectra of Ref. 18, but that work was carried out on single crystals and may not have been fully directionally averaged. XAS [53], x-ray Raman [54], and electron energy loss [55] experiments have all shown the sensitivity of this peak to orientation. There is, however, some uncertainty in the correction of our XAS to account for self-absorption effects.

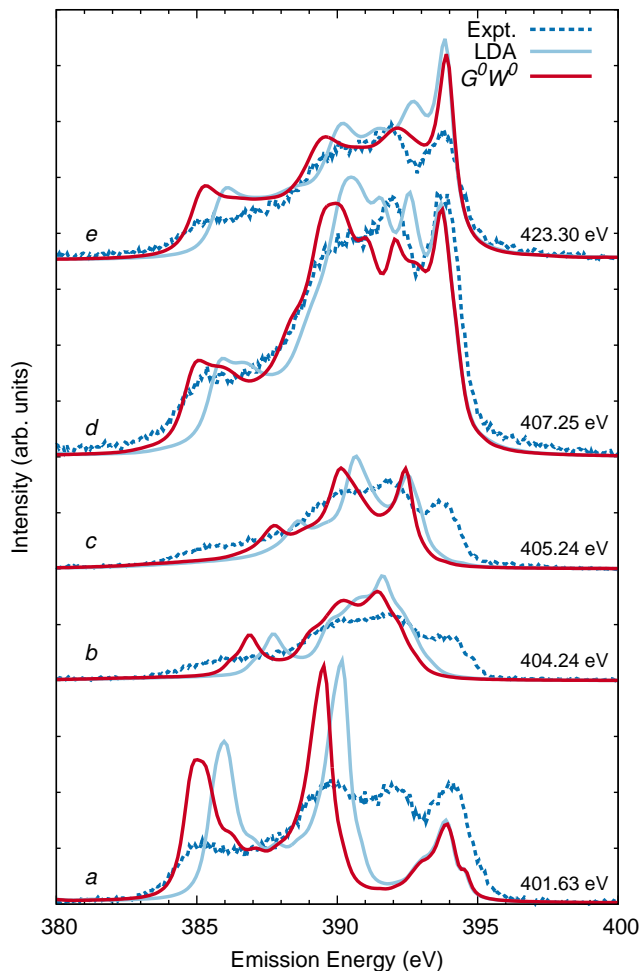


FIG. 5. (color online) The nitrogen K-edge RIXS of *h*-BN as measured (blue, dotted) and BSE calculations using LDA energies (light-blue, solid) and G^0W^0 energies (red, solid). (All of the BSE calculations use the LDA electron orbitals.) Plots are labeled sequentially by letter (Fig. 4) and by incident photon energy, and they are offset vertically for clarity. The experimental spectra have been normalized to correct for self-absorption effects, and experimental spectra *b* and *d* have been scaled by factors of 1.5x and 1.9x.

2. RIXS

X-ray emission spectra were taken at each of the energies marked in Fig. 4. Additional spectra were taken between point *d* (407.25 eV) and point *e* (425.30 eV), but those emission spectra were nearly indistinguishable from the spectrum at *e* except for changes in total count rate proportional to the changes in absorption. At energies well above the edge, x-ray emission spectra do not change shape with respect to changes in incident photon energy. This is called the non-resonant limit. We attribute the relatively quick transition to non-resonant x-ray emission in *h*-BN, within 8 eV of the absorption onset, to strong phonon coupling to the exciton, which

is well-known in *h*-BN from valence spectroscopy, e.g., [3, 56].

This transition is affected by several factors, but all of them serve to reduce the coherence of the excitation or the \mathbf{k} -space localization of the core hole in the intermediate excited state. Far above the Fermi level the conduction band states behave like nearly free electrons, and therefore the transition matrix elements from the initial core-level orbital will be nearly independent of \mathbf{k} . Additionally, lifetime broadening of the conduction band states will increase with distance from the Fermi level, generally becoming significant above the plasmon energy. This lifetime broadening (along with the core-hole broadening) yields an intermediate excited state that, depending on the amount of broadening, can mix together many conduction-electron-core-hole excitons with possibly very different \mathbf{k} -space distributions. Lastly, phonon scattering during RIXS, between absorption and emission, can both decouple the electron and hole momenta, normally constrained to conserve the momentum of the absorbed photon, and also destroy the coherence of the process. Ordinarily, if the final state of the system is a conduction-band-valence-hole exciton, without any changes to the vibrational states, intermediate states containing all possible core holes are summed over coherently. Conversely, if the final state contains some site-specific evidence of the intermediate state core-hole, such as localized vibrational excitations, then this requirement is lifted.

Continuing the investigation of section II B we calculated RIXS of the unit cell both using the LDA energies and then incorporating G^0W^0 corrections to the LDA energies of the occupied states (Fig. 5). Incorporating the G^0W^0 energies into the BSE calculation substantially improves the agreement of the highest energy RIXS spectra *d* and *e*. In *e* the spacing of the four main emission features closely matches the experiment. An apparent fifth feature in the LDA spectrum at 391.5 eV is not visible when GW corrections are included. The stronger GW correction to the σ bands is responsible for merging this feature into the lower π peak.

In the measured emission spectra *b* and *c* we see that the highest-energy feature near 394 eV is suppressed with respect to the *d* or *e*. This feature is associated with the π bands, and its absence in near-threshold RIXS of *h*-BN has been previously observed at both the boron [24, 25] and nitrogen edges [17]. The calculated spectra are more extreme, with the 394 eV peak completely absent for both *b* and *c*. The lowest peak at 385 eV, clearly visible in the calculated spectra of the other three energies is also absent for *b* and *c*, while in the measured spectra it is slightly reduced in strength. The behavior of the calculated spectra at these two energies broadly matches the trend of the measured spectra, with a reduction in spectral weight at both the 394 eV and 385 eV as compared to the non-resonant limit.

We carried out the same set of RIXS calculations on our ensemble of 8 disordered 64-atom supercells as for

the XAS, but due to the increased size we did not include *GW* corrections. In Fig. 6 we compare the ordered and disordered RIXS (using LDA energies) to the measured spectra. Unsurprisingly, the spectra from the disordered cells are generally broader than those from the ordered cell. Spectra *b* and *c* show very dramatic changes with the inclusion of initial-state disorder. The previously absent peaks at 394 eV and 386 eV (using LDA energies) are filled in. The same effect is present in disordered calculation of spectrum *a*, where spectral weight is filled in around 392 eV. The variation in emission spectra with incident photon energy is reduced by the disorder in the system, but the calculated spectra continue to show a much stronger excitation-energy dependence than the measured emission. The emission spectra show a large proportion of non-resonant x-ray emission, over which small changes are visible.

IV. CONCLUDING REMARKS

We can align valence band energies accurately once we include the *GW* corrections, improving the calculated RIXS spectra of *h*-BN. The incorporation of disorder clearly produces a more realistic representation of the x-ray emission. Combining the two corrections is currently too expensive computationally, but points the way to the necessary treatment. Further work is needed to expand the OCEAN framework to include intermediate-state phonon scattering.

Electronic structure calculations using DFT within the LDA adequately represent the dispersion of the valence bands in *h*-BN, as compared to *GW* calculations, but fail to correctly space them. Including self-energy corrections lowers the bonding σ bands by 0.8 eV as compared to the π bands, whereas the deeper non-bonding σ bands are lowered further by around 1.5 eV. Combining G^0W^0 corrections from the unit cell with the effects of atomic disorder yielded a band-gap correction consistent with experiment, but we did not account for how the presence of disorder might modify the self-energy corrections.

The BSE calculations of the x-ray absorption are in much improved agreement with the experimental measurement once disorder is taken into account via the phonon-mode method. However, the BSE calculations of RIXS show significantly more variation with incident energy than the measured emission spectra. Shifts in spectral weight are consistent between theory and experiment, with the measured RIXS including a large component of non-resonant emission, resulting in the reduced variation. This points to strong phonon coupling in the intermediate core-hole excited state which is currently neglected in our calculations. This phenomenon is well known [57, 58], but difficult to calculate in extended systems with many electronic and vibrational states. Several studies of x-ray emission have included the response of the nuclei to a core excitation, falling broadly into two categories.

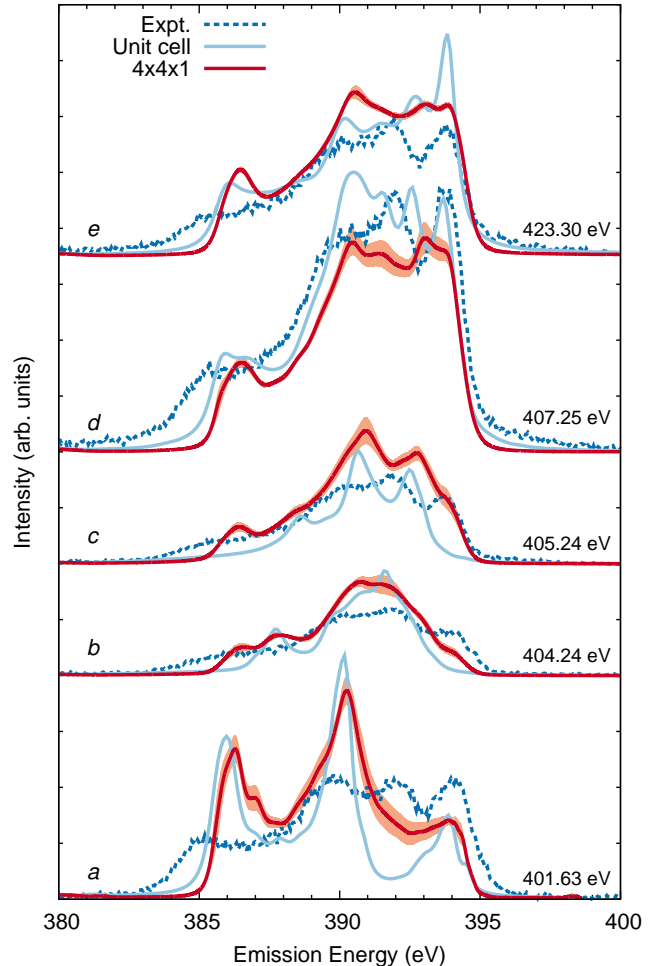


FIG. 6. (color online) The nitrogen K-edge RIXS of *h*-BN as measured (blue, dotted) and calculated with the BSE on top of LDA energies for the unit cell (light blue, solid) and an ensemble of 8 disordered $4 \times 4 \times 1$ (64-atom) supercells (red, solid). Statistical uncertainty ($\pm 2\Delta\sigma$) in the average of the disordered spectra are shown in orange shading. Plots are labeled by letter (see Fig. 4) and by incident photon energy, and they are offset vertically for clarity. Experimental spectra *b* and *d* have been scaled by factors of 1.5x and 1.9x.

In the first, liquids, both H_2O [59] and aqueous NH_3 [60, 61], have been investigated using *ab initio* molecular dynamics simulations. Briefly a $1s$ core-hole is created on the absorbing atom (O or N) and the excited electron can either be included or removed from the system entirely, representing near-edge RIXS and non-resonant XES, respectively. The nuclei and electronic states are allowed to follow the Born-Oppenheimer potential energy surface for a short time (20 fs), and x-ray emission spectra are calculated for each snapshot and weighted against the core-hole lifetime to determine the total x-ray emission spectrum. This approach necessarily neglects the coherent sum over possible core holes, instead choosing a single absorbing atom. Given both the initial disorder

of liquids and the large atomic motion induced by the core hole, this approximation is valid. Currently, this method is limited to treating the movement of the nuclei classically.

A second class of approaches has gained traction for calculating indirect RIXS of cuprates and related materials [62–64]. In contrast to *direct* RIXS (the subject of this paper), *indirect* RIXS probes low-loss excitations such as phonon scattering or *dd*-excitations. While differing in their details, this class of approaches treat electron-phonon interactions via explicit coupling between enumerated electron and vibrational states. Limitations are placed on the number of important electron bands and phonon modes to ensure this enumeration remains tractable. For indirect RIXS, with the initial XAS excitation detuned below the exciton, a model containing only a few conduction bands or impurity levels is likely sufficient. Importantly, for highly correlated materials, the electron-phonon coupling constants are not available from *ab initio* calculations like DFT, but are instead extracted by comparing RIXS measurements to calculations. Improving non-parametrized approaches like the BSE method to include phonon scattering, albeit on less highly-correlated systems, may provide a useful critique for improving these models.

As a rough approximation, the ratio of incoherent

emission to RIXS is dependent on the relation between the exciton lifetime and the phonon relaxation time [20]. At threshold the exciton lifetime is equal to the core-hole lifetime, and the phonon relaxation time is given by the Debye temperature. Using this ratio, the XES and RIXS can be averaged together [65]. However, this neglects any state-dependence or directionality of the electron-phonon coupling.

To adequately simulate phonon effects in RIXS with OCEAN it will be necessary to extend the current, coherent momentum-space approach to allow for the electron or hole to scatter. One option would be to consider the phonon excitations by way of a spectral function. The quasiparticles in the BSE, both electrons and holes, could be dressed to include phonon effects through the self-energy [66] or electron-phonon cumulant [67]. Alternatively, by exploiting the local nature of near-edge x-ray absorption, we could explicitly include a few local vibrational modes in the excited-state Hamiltonian [68]. A brute force expansion of the BSE basis to include phonons will increase the dimension of the Hamiltonian by the number of modes times the number of vibrational occupation levels required, which is too large to be practical at present. Balancing the trade off between accuracy and feasibility for including phonon contributions to RIXS in extended systems requires further study.

-
- ¹ A. Rubio, J. L. Corkill, and M. L. Cohen, Phys. Rev. B **49**, 5081 (1994).
 - ² N. G. Chopra, R. J. Luyken, K. Cherrey, V. H. Crespi, M. L. Cohen, S. G. Louie, and A. Zettl, Science **269**, 966 (1995).
 - ³ G. Cassaboies, P. Valvin, and B. Gil, Nature Photonics **10**, 262 (2016).
 - ⁴ T. C. Doan, J. Li, J. Y. Lin, and H. X. Jiang, Appl. Phys. Lett. **109**, 122101 (2016).
 - ⁵ G. Constantinescu, A. Kuc, and T. Heine, Phys. Rev. Lett. **111**, 036104 (2013).
 - ⁶ A. Zunger, A. Katzir, and A. Halperin, Phys. Rev. B **13**, 5560 (1976).
 - ⁷ J. Robertson, Phys. Rev. B **29**, 2131 (1984).
 - ⁸ Y.-N. Xu and W. Y. Ching, Phys. Rev. B **44**, 7787 (1991).
 - ⁹ J. Furthmüller, J. Hafner, and G. Kresse, Phys. Rev. B **50**, 15606 (1994).
 - ¹⁰ X. Blase, A. Rubio, S. G. Louie, and M. L. Cohen, Phys. Rev. B **51**, 6868 (1995).
 - ¹¹ B. Arnaud, S. Lebègue, P. Rabiller, and M. Alouani, Phys. Rev. Lett. **96**, 026402 (2006).
 - ¹² E. Tegeler, N. Kosuch, G. Wiech, and A. Faessler, Phys. Status Solidi B **91**, 223 (1979).
 - ¹³ A. Mansour and S. E. Schnatterly, Phys. Rev. B **36**, 9234 (1987).
 - ¹⁴ H. Ma, S. H. Lin, R. W. Carpenter, P. Rice, and O. F. Sankey, J. Appl. Phys. **73**, 7422 (1993).
 - ¹⁵ W. L. O'Brien, J. Jia, Q.-Y. Dong, T. A. Callcott, K. E. Miyano, D. L. Ederer, D. R. Mueller, and C.-C. Kao, Phys. Rev. Lett. **70**, 238 (1993).
 - ¹⁶ J. J. Jia, T. A. Callcott, E. L. Shirley, J. A. Carlisle, L. J. Terminello, A. Asfaw, D. L. Ederer, F. J. Himpsel, and R. C. C. Perera, Phys. Rev. Lett. **76**, 4054 (1996).
 - ¹⁷ N. Miyata, M. Yanagihara, M. Watanabe, Y. Harada, and S. Shin, J. Phys. Soc. Jpn. **71**, 1761 (2002).
 - ¹⁸ J. B. MacNaughton, A. Moewes, R. G. Wilks, X. T. Zhou, T. K. Sham, T. Taniguchi, K. Watanabe, C. Y. Chan, W. J. Zhang, I. Bello, S. T. Lee, and H. Hofsäss, Phys. Rev. B **72**, 195113 (2005).
 - ¹⁹ Y. Ma, N. Wassdahl, P. Skytt, J. Guo, J. Nordgren, P. D. Johnson, J.-E. Rubensson, T. Boske, W. Eberhardt, and S. D. Kevan, Phys. Rev. Lett. **69**, 2598 (1992).
 - ²⁰ Y. Ma, Phys. Rev. B **49**, 5799 (1994).
 - ²¹ E. L. Shirley, Phys. Rev. Lett. **80**, 794 (1998).
 - ²² J. A. Carlisle, E. L. Shirley, L. J. Terminello, J. J. Jia, T. A. Callcott, D. L. Ederer, R. C. C. Perera, and F. J. Himpsel, Phys. Rev. B **59**, 7433 (1999).
 - ²³ E. L. Shirley, J. Electron Spectrosc. Relat. Phenom. **110-111**, 305 (2000).
 - ²⁴ M. Yanagihara, N. Miyata, T. Ejima, M. Watanabe, and Y. Kayanuma, J. Phys. Soc. Jpn. **66**, 1626 (1997).
 - ²⁵ K. Noba, Y. Kayanuma, and M. Yanagihara, J. Phys. Soc. Jpn. **67**, 664 (1998).
 - ²⁶ R. W. G. Wyckoff, *Crystal Structures* (1963).
 - ²⁷ J. Vinson, T. Jach, W. T. Elam, and J. D. Denlinger, Phys. Rev. B **90**, 205207 (2014).
 - ²⁸ J. Vinson, T. Jach, M. Müller, R. Unterumsberger, and B. Beckhoff, Phys. Rev. B **94**, 035163 (2016).
 - ²⁹ R. Nemausat, D. Cabaret, C. Gervais, C. Brouder, N. Trcera, A. Bordage, I. Errea, and F. Mauri, Phys. Rev. B **92**, 144310 (2015).
 - ³⁰ P. Giannozzi, S. Baroni, N. Bonini, M. Calandra, R. Car,

- C. Cavazzoni, D. Ceresoli, G. L. Chiarotti, M. Cococcioni, I. Dabo, *et al.*, J. Phys. Condens. Matter **21**, 395502 (2009); www.quantum-espresso.org.
- ³¹ P. Giannozzi, S. de Gironcoli, P. Pavone, and S. Baroni, Phys. Rev. B **43**, 7231 (1991).
- ³² K. F. Garrity, J. W. Bennett, K. M. Rabe, and D. Vanderbilt, Comput. Mater. Sci. **81**, 446 (2014), (v. 1.5).
- ³³ J. P. Perdew and A. Zunger, Phys. Rev. B **23**, 5048 (1981).
- ³⁴ G. Kern, G. Kresse, and J. Hafner, Phys. Rev. B **59**, 8551 (1999).
- ³⁵ J. Serrano, A. Bosak, R. Arenal, M. Krisch, K. Watanabe, T. Taniguchi, H. Kanda, A. Rubio, and L. Wirtz, Phys. Rev. Lett. **98**, 095503 (2007).
- ³⁶ R. Cuscó, B. Gil, G. Cassaboïs, and L. Artús, Phys. Rev. B **94**, 155435 (2016).
- ³⁷ L. Hedin, Phys. Rev. **139**, A796 (1965).
- ³⁸ G. Cappellini, V. Fiorentini, K. Tenelsen, and F. Bechstedt, "Gallium nitride and related materials," in *Materials Research Society Symposium - Proceedings*, edited by R. D. Dupuis, J. A. Edmond, F. A. Ponce, and S. Nakamura (Materials Research Society, 1996) p. 429.
- ³⁹ S.-P. Gao, Solid State Comm. **152**, 1817 (2012).
- ⁴⁰ H. Henck, D. Pierucci, G. Fugallo, J. Avila, G. Cassaboïs, Y. J. Dappe, M. G. Silly, C. Chen, B. Gil, M. Gatti, F. Sottile, F. Sirotti, M. C. Asensio, and A. Ouerghi, Phys. Rev. B **95**, 085410 (2017).
- ⁴¹ X. Gonze, F. Jollet, F. A. Araujo, D. Adams, B. Amadon, T. Applencourt, C. Audouze, J.-M. Beuken, J. Bieder, A. Bokhanchuk, E. Bousquet, F. Bruneval, D. Caliste, M. Cote, F. Dahm, F. D. Pieve, M. Delaveau, M. D. Gennar, B. Dorado, C. Espejo, G. Geneste, L. Genovese, A. Gerossier, M. Giantomassi, Y. Gillet, D. R. Hamann, L. He, G. Jomard, J. L. Janssen, S. L. Roux, A. Levitt, A. Lherbier, F. Liu, I. Lukacevic, A. Martin, C. Martins, M. J. T. Oliveira, S. Ponce, Y. Pouillon, T. Rangel, G.-M. Rignanese, A. H. Romero, B. Rousseau, O. Rubel, A. A. Shukri, M. Stankovski, M. Torrent, M. J. V. Setten, B. V. Troeye, M. J. Verstraete, D. Waroquier, J. Wiktor, B. Xue, A. Zhou, and J. W. Zwanziger, Comput. Phys. Comm. **205**, 106 (2016); The ABINIT code is a common project of the Université Catholique de Louvain, Corning Incorporated, and other contributors; www.abinit.org.
- ⁴² A. A. Mostofi, J. R. Yates, Y.-S. Lee, I. Souza, D. Vanderbilt, and N. Marzari, Comput. Phys. Comm. **178**, 685 (2008).
- ⁴³ F. Senf, U. Flechsigs, F. Eggenstein, W. Gudat, R. Klein, H. Rabus, and G. Ulm, J. Synchrotron Radiat. **5**, 780 (1998).
- ⁴⁴ F. Scholze, B. Beckhoff, G. Brandt, R. Fliegauf, R. Klein, B. Meyer, D. Rost, D. Schmitz, M. Veldkamp, J. Weser, G. Ulm, E. Louis, A. E. Yakshin, S. Oestreich, and F. Biskerk, Proc. SPIE **4146**, 72 (2000).
- ⁴⁵ M. Müller, B. Beckhoff, R. Fliegauf, and B. Kanngießer, Phys. Rev. A **79**, 032503 (2009).
- ⁴⁶ J. Vinson, J. J. Rehr, J. J. Kas, and E. L. Shirley, Phys. Rev. B **83**, 115106 (2011).
- ⁴⁷ K. Gilmore, J. Vinson, E. Shirley, D. Prendergast, C. Pemmaraaju, J. Kas, F. Vila, and J. Rehr, Comput. Phys. Comm. **197**, 109 (2015).
- ⁴⁸ OPIUM pseudopotential package v3.8. <http://opium.sourceforge.net>.
- ⁴⁹ R. Geick, C. H. Perry, and G. Rupprecht, Phys. Rev. **146**, 543 (1966).
- ⁵⁰ D. A. Evans, A. G. McGlynn, B. M. Towlson, M. Gunn, D. Jones, T. E. Jenkins, R. Winter, and N. R. J. Poolton, J. Phys. Condens. Matter **20**, 075233 (2008).
- ⁵¹ K. Watanabe, T. Taniguchi, and H. Kanda, Nat. Mater. **3**, 404 (2004).
- ⁵² L. Wirtz, A. Marini, and A. Rubio, Phys. Rev. Lett. **96**, 126104 (2006).
- ⁵³ J. Moscovici, G. Loupías, P. Parent, and G. Tourillon, J. Phys. Chem. Solids **57**, 1159 (1996).
- ⁵⁴ N. Watanabe, H. Hayashi, Y. Udagawa, K. Takeshita, and H. Kawata, Appl. Phys. Lett. **69**, 1370 (1996).
- ⁵⁵ R. Arenal, M. Kociak, and N. J. Zaluzec, Appl. Phys. Lett. **90**, 204105 (2007).
- ⁵⁶ K. Watanabe and T. Taniguchi, Phys. Rev. B **79**, 193104 (2009).
- ⁵⁷ G. D. Mahan, Phys. Rev. B **15**, 4587 (1977).
- ⁵⁸ C.-O. Almbladh, Phys. Rev. B **16**, 4343 (1977).
- ⁵⁹ M. Odelius, H. Ogasawara, D. Nordlund, O. Fuchs, L. Weinhardt, F. Maier, E. Umbach, C. Heske, Y. Zubavichus, M. Grunze, J. D. Denlinger, L. G. M. Pettersson, and A. Nilsson, Phys. Rev. Lett. **94**, 227401 (2005).
- ⁶⁰ L. Weinhardt, M. Weigand, O. Fuchs, M. Bär, M. Blum, J. D. Denlinger, W. Yang, E. Umbach, and C. Heske, Phys. Rev. B **84**, 104202 (2011).
- ⁶¹ L. Weinhardt, E. Ertan, M. Iannuzzi, M. Weigand, O. Fuchs, M. Bar, M. Blum, J. D. Denlinger, W. Yang, E. Umbach, M. Odelius, and C. Heske, Phys. Chem. Chem. Phys. **17**, 27145 (2015).
- ⁶² J. J. Lee, B. Moritz, W. S. Lee, M. Yi, C. J. Jia, A. P. Sorini, K. Kudo, Y. Koike, K. J. Zhou, C. Monney, V. Strocov, L. Patthey, T. Schmitt, T. P. Devereaux, and Z. X. Shen, Phys. Rev. B **89**, 041104 (2014).
- ⁶³ L. J. P. Ament, M. van Veenendaal, and J. van den Brink, Europhys. Lett. **95**, 27008 (2011).
- ⁶⁴ T. P. Devereaux, A. M. Shvaika, K. Wu, K. Wohlfeld, C. J. Jia, Y. Wang, B. Moritz, L. Chaix, W.-S. Lee, Z.-X. Shen, G. Ghiringhelli, and L. Braicovich, Phys. Rev. X **6**, 041019 (2016).
- ⁶⁵ J. Vinson, *Bethe-Salpeter Equation Approach for Calculations of X-ray Spectra*, Ph.D. thesis, University of Washington (2012).
- ⁶⁶ F. Giustino, Rev. Mod. Phys. **89**, 015003 (2017).
- ⁶⁷ S. M. Story, J. J. Kas, F. D. Vila, M. J. Verstraete, and J. J. Rehr, Phys. Rev. B **90**, 195135 (2014).
- ⁶⁸ K. Gilmore and E. L. Shirley, J. Phys. Condens. Matter **22**, 315901 (2010).